Radiation and Dissipation of Internal Waves Generated by Geostrophic Motions Impinging on Small-Scale Topography: Application to the Southern Ocean

MAXIM NIKURASHIN* AND RAFFAELE FERRARI

Massachusetts Institute of Technology, Cambridge, Massachusetts

(Manuscript received 16 July 2009, in final form 8 April 2010)

ABSTRACT

Recent estimates from observations and inverse models indicate that turbulent mixing associated with internal wave breaking is enhanced above rough topography in the Southern Ocean. In most regions of the ocean, abyssal mixing has been primarily associated with radiation and breaking of internal tides. In this study, it is shown that abyssal mixing in the Southern Ocean can be sustained by internal waves generated by geostrophic motions that dominate abyssal flows in this region. Theory and fully nonlinear numerical simulations are used to estimate the internal wave radiation and dissipation from lowered acoustic Doppler current profiler (LADCP), CTD, and topography data from two regions in the Southern Ocean: Drake Passage and the southeast Pacific. The results show that radiation and dissipation of internal waves generated by geostrophic motions reproduce the magnitude and distribution of dissipation previously inferred from finescale measurements in the region, suggesting that it is one of the primary drivers of abyssal mixing in the Southern Ocean.

1. Introduction

Ocean mixing sets the stratification of much of the global ocean by the upwelling of dense, deep waters formed in polar regions (Wunsch and Ferrari 2004). Mixing is especially important in the Southern Ocean where the meridional overturning circulation (MOC) of the global ocean is largely powered. However, little is known about what dynamics supports that mixing.

The Southern Ocean limb of the MOC can be described as being composed of an upper and a lower cell (Speer et al. 2000). Theories suggest that the upper cell is driven by atmospheric forcing at the surface with an adiabatic return flow at depth (Rintoul et al. 2001; Marshall and Radko 2003; Olbers et al. 2004). Much less is known about the dynamics of the lower cell, except that diabatic mixing is essential to explain the latitudinal change in deep water mass properties (Ito and Marshall 2008). Inverse analyses of the Southern Ocean hydrography confirm that high mixing rates in the deep Southern Ocean are required to close the heat and salt budgets (Ganachaud and Wunsch 2000; Sloyan and Rintoul 2001). Enhanced abyssal mixing has been linked to the radiation of internal tides in other parts of the ocean (Polzin et al. 1997; Ledwell et al. 2000; St. Laurent and Garrett 2002). However, this does not seem to be the case in the Southern Ocean where abyssal flows are dominated by geostrophic eddies (Naveira Garabato et al. 2003). Nikurashin and Ferrari (2010) showed that geostrophic motions are very efficient at radiating waves from small topographic features, resulting in local mixing. Polzin and Firing (1997) also found that abyssal mixing appears to be enhanced in regions of strong geostrophic flows. Here, we test the hypothesis that the abyssal mixing observed in the Southern Ocean can be explained by radiation and breaking of waves resulting from geostrophic flows impinging on small-scale topography.

Estimates of turbulent mixing inferred from lowered acoustic Doppler current profiler (LADCP) and CTD data (Polzin and Firing 1997; Naveira Garabato et al. 2004) using finescale parameterizations (Gregg 1989; Polzin et al. 1995) confirm the inference from large-scale budgets that in the Southern Ocean turbulent kinetic energy dissipation and diapycnal mixing are enhanced by orders of magnitude above the background values

* Current affiliation: Princeton University/GFDL, Princeton, New Jersey.

Corresponding author address: Maxim Nikurashin, Princeton University/GFDL, 201 Forrestal Rd., Princeton, NJ 08540.
E-mail: man@alum.mit.edu

DOI: 10.1175/2010JPO4315.1

typically found in the ocean. The estimated diapycnal mixing is enhanced primarily within a kilometer above the bottom, only where the topography is rough. For example, the vertically integrated dissipation rate averaged for a few stations across the rough topography of Drake Passage is reported to be of $O(10)$ mW m^{-2}, corresponding to a bottom diapycnal diffusivity of $O(10^{-2})$ m^2 s^{-1} (Naveira Garabato et al. 2004). In the southeast Pacific, where topography is smooth, the vertically integrated dissipation rate is lower, $O(1)$ mW m^{-2}. A. Naveira Garabato (2008, personal communication) quotes a two- to threefold uncertainty in these estimates, which is substantially smaller than the order of magnitude difference between the values in the Drake Passage and those in the southeast Pacific regions of the Southern Ocean.

Kunze et al. (2006), applying a similar finescale parameterization to a larger number of full-depth LADCP profiles collected during the World Ocean Circulation Experiment (WOCE), find lower values of the energy dissipation rate and diapycnal diffusivity in the same regions. Kunze et al. (2006) estimate lower values, because they make more conservative assumptions about the LADCP noise–signal ratio and low-pass filter shear in regions of weak stratification. However, the main conclusion stands: mixing is enhanced in regions with rough topography and it is correlated with the magnitude of the bottom flow. The question arises as to what is the source of the internal waves that break and mix.

Moored observations (Nowlin et al. 1986) show that the bulk of the kinetic energy of the horizontal motions in Drake Passage is in subinertial flows, while only about 20% of the kinetic energy is in fluctuations between the inertial and stratification frequencies, including inertial oscillations, tides, and the internal wave continuum. Any one of these motions can generate internal waves through interaction with bottom topography. However, theories of topographic wave generation have focused on the barotropic tidal component, which is believed to dominate wave radiation in the midlatitudes (e.g., Bell 1975a; Llewellyn Smith and Young 2002; Khatiwala 2003; Garrett and Kunze 2007). Wave generation by the dominant M_2 tidal component is estimated globally by Nycander (2005) using the linear theory developed by Llewellyn Smith and Young (2002), tidal velocities from the global tidal model of Egbert and Erofeeva (2002), and bottom topography from satellite altimetry (Smith and Sandwell 1997). Using the tidal energy flux data, kindly provided to us by Dr. Nycander, we estimate that the tidal energy flux into the ocean interior from topography deeper than 2 km for Drake Passage is about 1–2 mW m^{-2}. Even if all this energy was dissipated locally, tides could only support one-tenth of the dissipation of $O(10)$ mW m^{-2} estimated in Drake Passage. Nikurashin and Ferrari (2010) showed that geostrophic flows impinging upon rough topography are very efficient generators of turbulent mixing. Using idealized numerical simulations with parameters characteristic of Drake Passage, they predicted energy dissipation rates up to 20 mW m^{-2}.

In this paper we extend the theoretical framework developed in Nikurashin and Ferrari (2010) to estimate internal wave generation by geostrophic flows in Drake Passage and the southeast Pacific. In section 2, we describe the available velocity, stratification, and topography data. An analytical representation of the topography spectrum is also presented and discussed. In section 3, we review the linear theory of wave radiation by geostrophic flows for arbitrary topography. In section 4, we present the energy conversion estimates. In section 5, we test the theoretical estimates versus numerical simulations and observations. Energy dissipation estimates are presented in section 6. Finally, results are summarized in section 7.

2. Data

The characteristics of waves radiated by a geostrophic flow impinging on topography depend on the spectrum of short topographic hills as well as the bottom values of the geostrophic velocity and stratification. Geostrophic velocities and topography data are available for two different regions of the Southern Ocean: Drake Passage and the southeast Pacific. These two regions are characterized, respectively, by high and low rates of abyssal mixing. A major goal of this paper is to test whether wave radiation theory can reproduce the observed magnitudes and spatial variations of abyssal mixing in these two regions.

a. Geostrophic flow and stratification characteristics

Bottom velocity and stratification are estimated with LADCP and CTD data from sections across western Drake Passage and in the southeast Pacific (Fig. 1). Velocity and hydrographic sections across Drake Passage were collected as a part of the Antarctic Large-Scale Box Analysis and the Role of the Scotia Sea (ALBATROSS) cruise during March 1999. Details of the data collection and analysis methods are given in Heywood and Stevens (2000), and a complete description of the CTD and LADCP observations is in Naveira Garabato et al. (2002, 2003). Velocity and hydrography data used for the southeast Pacific region were collected during WOCE along the P18 line (Kunze et al. 2006).

Wunsch (1997) found, from mooring data, that the bulk of the geostrophic velocity is in low vertical modes (barotropic and baroclinic mode one). At high modes, there is a substantial amount of internal gravity wave energy.

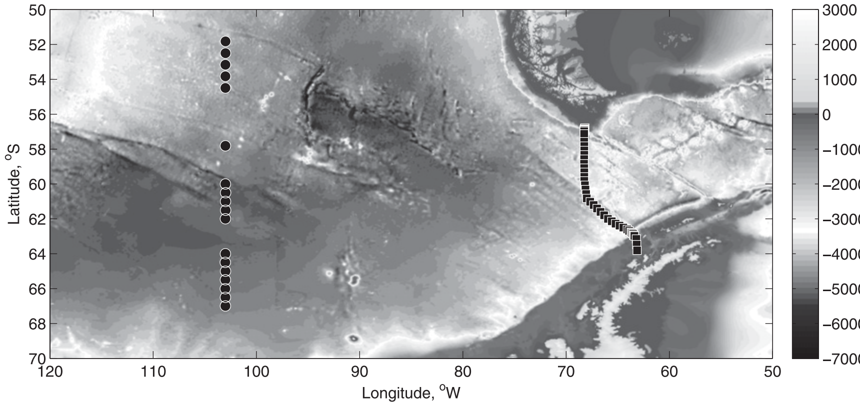

FIG. 1. Bathymetry of the Southern Ocean region around Drake Passage. CTD and LADCP stations from the ALBATROSS section in Drake Passage and along the P18 section in the southeast Pacific are represented by squares and circles, respectively.

A. Naveira Garabato (2008, personal communication) compared geostrophic and averaged LADCP shear and concluded that in the ALBATROSS and P18 sections the geostrophic signal dominates at scales larger than 100–200 m, while smaller scales are dominated by internal waves. We define the bottom geostrophic velocity and stratification as the averages over the bottom 500 m, a scale large enough to filter out internal wave signals.

The uncertainty in the direction of the flow, due to errors in the LADCP compass heading of ~5° (A. Naveira Garabato 2005, personal communication), is not an issue for the calculation presented below because, due to a lack of information on the flow-topography orientation, we consider all possible flow orientations rather than the particular flow direction found in the data. The magnitude of the instrument noise of $O(1)$ cm s^{-1} (A. Naveira Garabato 2008, personal communication) is also small and does not influence the calculation presented below.

The geostrophic velocity, defined as the 100-m low-passed LADCP velocity, in Drake Passage is dominated by the Antarctic Circumpolar Current (ACC) fronts, peaking at the surface of the ocean, decaying in the upper kilometer (the thermocline) and remaining essentially constant below (Fig. 2). Surface velocities of up to 50 cm s^{-1} are associated with the Sub-Antarctic Front, the Polar Front, and the South ACC Front. The corresponding

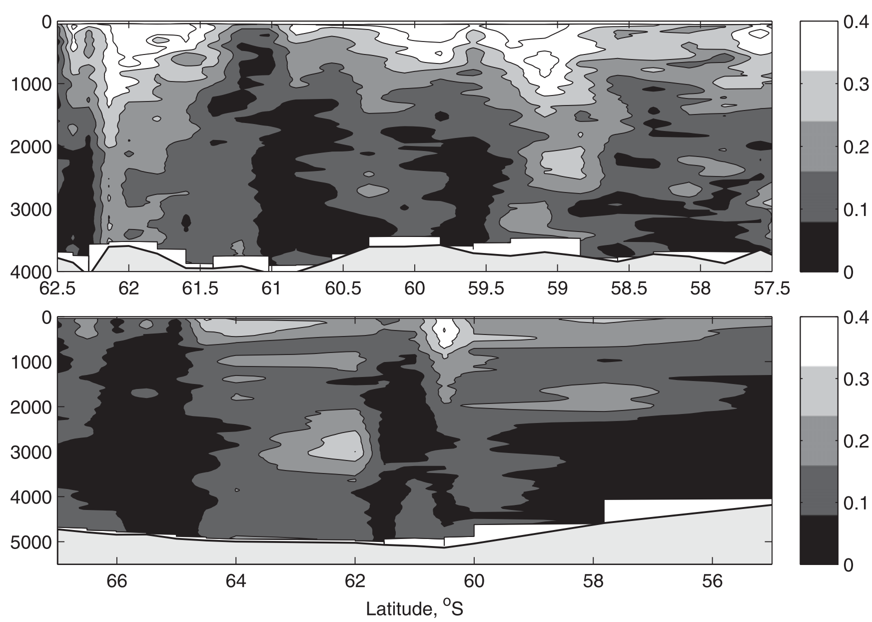

FIG. 2. Flow speed (m s^{-1}), defined as the 100-m low-passed LADCP velocity, from (top) the ALBATROSS section in Drake Passage and from (bottom) the P18 section in the southeast Pacific.

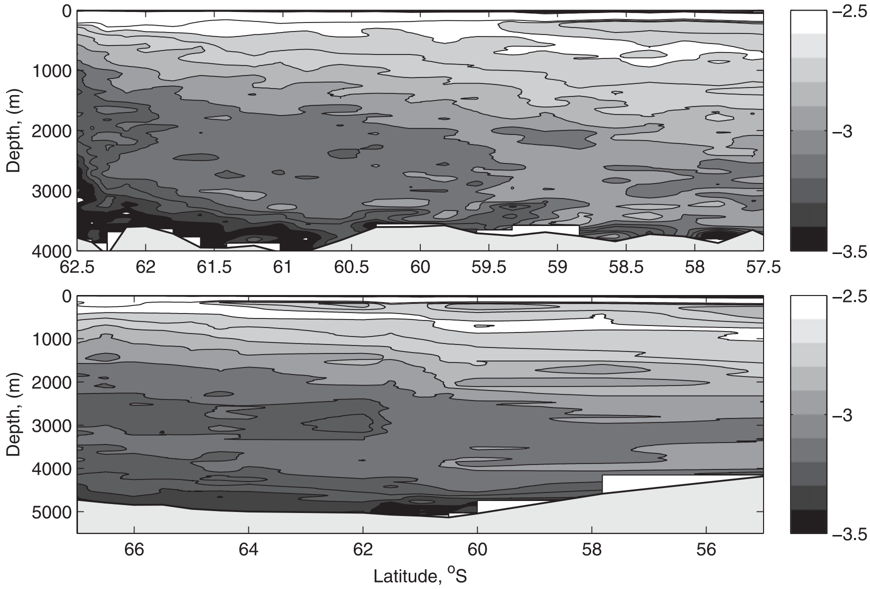

FIG. 3. Buoyancy frequency (s^{-1}) in logarithmic scale from (top) the ALBATROSS section in Drake Passage and from (bottom) the P18 section in the southeast Pacific.

bottom velocities reach up to 10–20 cm s^{-1}. Outside the fronts, bottom velocities are smaller $\simeq$(1–2) cm s^{-1}. Stations in Drake Passage have a spacing of $\simeq$30 km.

The potential density stratification in Drake Passage, derived from CTD temperature and salinity data, decays with depth in the thermocline while it is nearly uniform in the abyss (Fig. 3). There are, however, latitudinal variations. Bottom values of stratification $N^2 = -g/\rho_0 \partial\rho/\partial z$, where ρ is the potential density, g is the gravity, and ρ_0 is a reference value, range from 10^{-3} s^{-1} north of Drake Passage to 0.5×10^{-3} s^{-1} in the south (Fig. 4). The stratification is close to 10^{-3} s^{-1} in the Polar ACC Front,

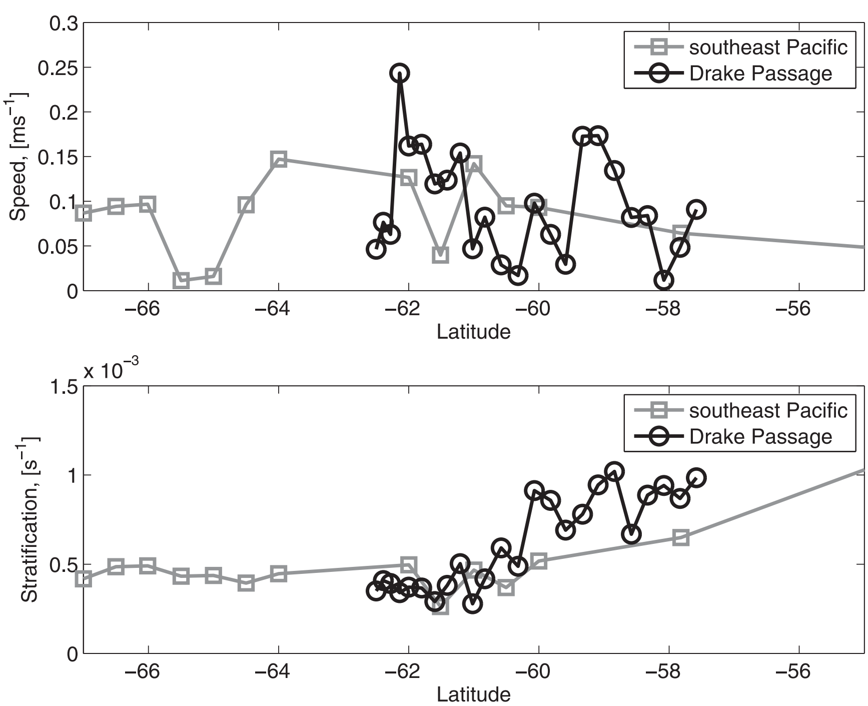

FIG. 4. (top) Bottom speed (m s^{-1}) and (bottom) stratification (s^{-1}) for the Drake Passage and the southeast Pacific regions.

the region where the bottom velocity and wave radiation are largest.

Sections in the southeast Pacific (Figs. 2 and 3) were collected in clusters separated by $\simeq$200 km; the stations within each cluster had a spacing of $\simeq$55 km. Bottom values of velocity and stratification in the 67°–55°S latitudinal range are close to those in Drake Passage. The stratification varies from 0.5×10^{-3} s^{-1} in the south to about 0.7×10^{-3} s^{-1} in the north. The bottom velocity decreases equatorward from about 15 to 5 cm s^{-1} without a clear signature of the ACC fronts, which is probably an artifact of the coarser sampling grid.

b. Topography characteristics

According to linear theory, a mean flow with bottom velocity of U_0 and bottom stratification N can generate radiating internal waves from topographic scales k in the range

$$\frac{|f|}{U_0} < k < \frac{N}{U_0}. \tag{1}$$

For an inertial frequency $|f| = 10^{-4}$ s^{-1}, a value representative of the latitudes considered here, $U_0 = 10$ cm s^{-1} and $N = 10^{-3}$ s^{-1}; this interval spans wavelengths from about 600 m to 6 km. This raises a technical problem for estimating wave radiation from the data, because topographic features with scales shorter than 10–20 km are not well resolved by satellite bathymetry (Smith and Sandwell 1997) and are only available from ship soundings or high-resolution multibeam topography data.

Multibeam topography data are available in the Drake Passage region (R. Livermore, British Antarctic Survey, 2005, personal communication). The data superimposed on the bathymetry data from satellite altimetry (Smith and Sandwell 1997) are shown in Fig. 5. Bottom topography is dominated by ridges at scales larger than about 100 km. Abyssal hills at smaller scales are ubiquitous in the multibeam topography, but they are not visible in the satellite-based data.

We compute a characteristic two-dimensional topography spectrum by averaging the spectra from several different regions, up to 100 km × 100 km wide, covered by the multibeam topography data. The spectrum is normalized such that the integrated spectrum gives the topography mean square height:

$$\overline{h^2} = \frac{1}{4\pi^2}\int_{-\infty}^{+\infty}\int_{-\infty}^{+\infty} P(\mathbf{k})\, d\mathbf{k}, \tag{2}$$

where $P(\mathbf{k})$ is the topography spectrum and $\mathbf{k} = (k, l)$ is the horizontal wave vector. The two-dimensional spectrum of Drake Passage topography is shown in Fig. 6.

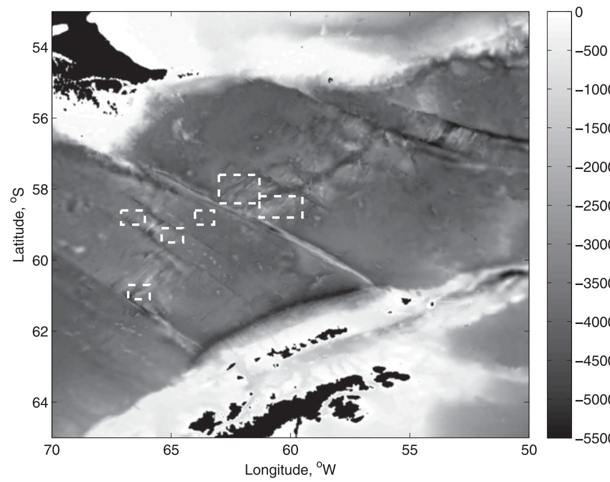

FIG. 5. Multibeam topography data (m, British Antarctic Survey) for the Drake Passage region superimposed on the bathymetry data from satellite altimetry (Smith and Sandwell 1997). The regions with multibeam topography data used to estimate the 2D model spectrum in (3) are shown by dashed rectangles.

The observed spectrum is well described by the model spectrum proposed by Goff and Jordan (1988), which is based on a statistical description of abyssal hills formed by ridge-crest processes, off-ridge tectonics, and vulcanism. Goff and Jordan (1988), through a survey of available high-resolution topographic data, concluded that a satisfactory representation of abyssal hills is given by the model spectrum:

$$P(\mathbf{k}) = \frac{2\pi\overline{h^2}(\mu-2)}{k_0 l_0}\left[1 + \frac{|\mathbf{k}|^2}{k_0^2}\cos^2(\phi-\phi_0) + \frac{|\mathbf{k}|^2}{l_0^2}\sin^2(\phi-\phi_0)\right]^{-\mu/2}, \tag{3}$$

where $|\mathbf{k}|$ is the horizontal wavenumber magnitude, ϕ is the angle between the wave vector and the eastward direction, $\overline{h^2}$ is the variance of the topographic height, k_0 and l_0 are the characteristic wavenumbers of the principal axes of anisotropy, ϕ_0 is the azimuthal angle, and μ is the high-wavenumber roll-off slope. [The μ parameter is related to the parameter ν used in Goff and Jordan (1988) as $\mu = 2(\nu + 1)$.] The model spectrum becomes flat at wavenumbers lower than $\sqrt{k_0^2 + l_0^2}$; this is the range of scale where abyssal hills transition into large-scale topographic features. At smaller scales the model spectrum rolls off anisotropically, the ratio of the major to minor axis being k_0/l_0. This anisotropy captures the tendency of abyssal hills to be oriented approximately perpendicular to the spreading direction of the large-scale ridges.

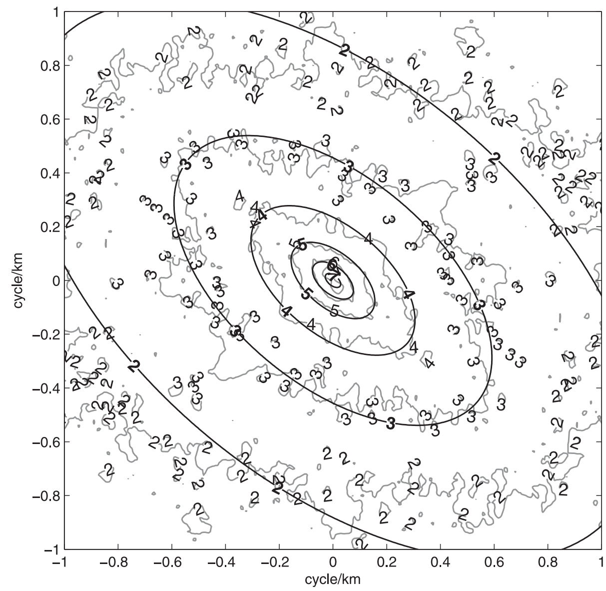

FIG. 6. The 2D topography spectrum estimated using multibeam topography data from the Drake Passage is shown as gray contours. The spectrum is in units of m^2 km^2 $cycle^{-2}$. The black contours represent the isolines of the 2D model spectrum in (3) with parameters chosen to best fit the observed spectrum. The model spectrum captures more than 90% of the observed spectrum variance in the characteristic lee wave radiation wavenumber range.

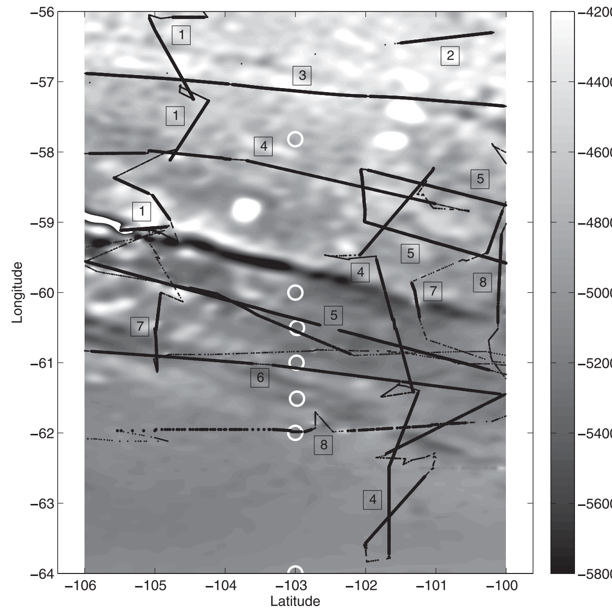

FIG. 7. Satellite bathymetry of the southeast Pacific region (m). The white circles show the position of the LADCP stations along the P18 section. The black lines are the sections along which high-resolution shipboard topographic data were used to fit the 1D model spectrum in (4). Numbers in boxes correspond to ship surveys described in Table 1.

The simple spectral model for abyssal hills given in (3) describes the statistical properties of abyssal hill topography at scales of $O(50)$ km and smaller (Goff and Jordan 1988). We use this model to characterize the abyssal hill topography on the range of radiative scales given by (1). The free parameters of the model spectrum are fitted in a least squares sense to the spectrum estimated from observations in Drake Passage. These parameters are the rms height of the topography, $(\overline{h^2})^{1/2} = 305$ m; the characteristic wavenumbers $k_0 = 2.3 \times 10^{-4}$ m^{-1} and $l_0 = 1.3 \times 10^{-4}$ m^{-1} of the principal axes of anisotropy; the azimuthal angle $\phi_0 = 320°$; and the high-wavenumber roll-off slope, $\mu = 3.5$. Figure 6 shows that this representation matches well the data at scales 1 km and larger, which dominate the wave radiation. The aspect ratio of the major to minor axis of the spectrum is 1.8, reflecting a slight anisotropy in the abyssal hills. The rms topographic height in the radiative wavenumber range given by (1), estimated using typical values of $U_0 = 10$ cm s^{-1} and $N = 10^{-3}$ s^{-1}, is 60 m. We do not report errors in the estimated parameters, because these errors are swamped by the unknown relative orientation of the topography and velocity in the radiation estimate presented below.

There are no high-resolution multibeam topography data available in the southeast Pacific region. In this region, we rely on available ship soundings (Fig. 7) from the U.S. National Geophysical Data Center (NGDC). We compute a characteristic one-dimensional spectrum (Fig. 8) as an average over 23 different spectra estimated along the ship tracks from eight surveys, as summarized in Table 1. The spectrum captures the transition from the plateau at topographic scales larger than about 30–40 km to a −2.5 roll off at the smaller scales.

We rely on the model of Goff and Jordan (1988) to extrapolate the spectrum down to the whole range of scales necessary for the wave radiation calculation. We fit a one-dimensional form of the model spectrum $P_{1D}(k)$ obtained by integrating (3) along the wavenumber component l, to the spectrum estimated from the data at scales that are resolved by the shipboard data. In case of isotropic topography, $k_0 = l_0 = \kappa_0$, the one-dimensional spectrum is

$$P_{1D}(k) = \overline{h^2}\kappa_0^{(\mu-2)}(\mu-2)B\left[\frac{1}{2}, \frac{(\mu-1)}{2}\right] \times (\kappa_0^2 + k^2)^{-(\mu-1)/2}, \quad (4)$$

where $B(1/2, (\mu - 1)/2)$ is the beta function. If the topography is anisotropic, then the one-dimensional spectrum has the same form, but the characteristic wavenumber κ_0 is a function of k_0, l_0 and the azimuth angle ϕ_0, that is, $\kappa_0 = \kappa_0(k_0, l_0, \phi_0)$.

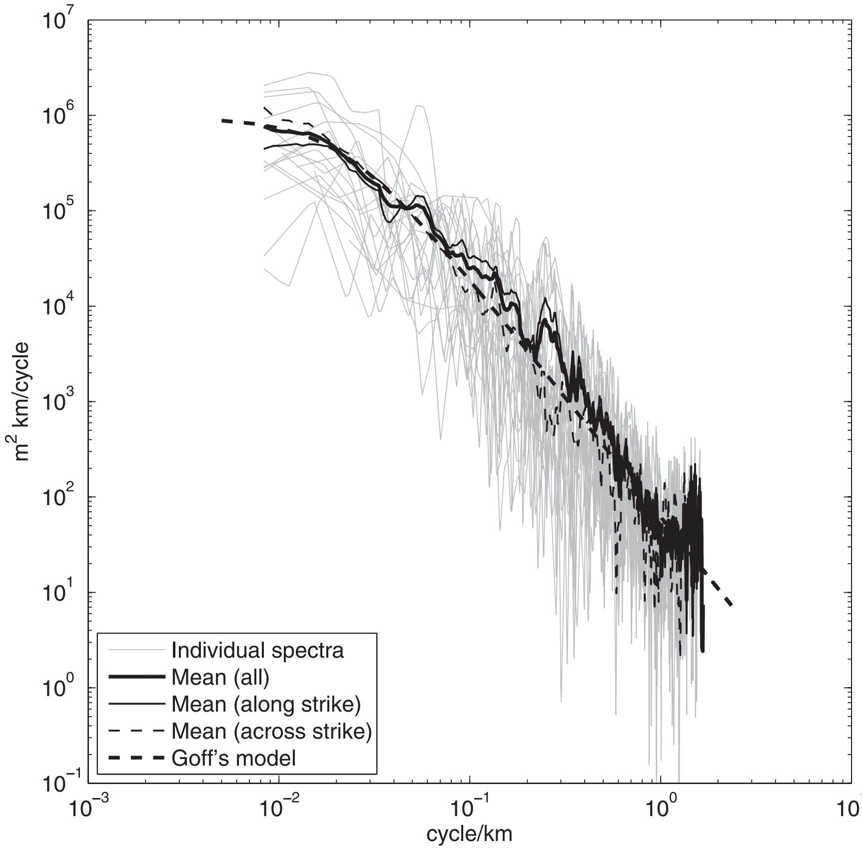

FIG. 8. One-dimensional topography spectrum estimated along ship tracks from the shipboard topography data. The thick black line is the average of the spectra from all tracks, while the thin continuous and dashed black lines are averages of the spectra from along- and across-strike profiles. Differences between the along- and across-strike lines are less than a factor of 2 and are inconsequential for radiation estimates. The thick dashed line is the least squares best-fit 1D model in (4).

We least squares fitted the model spectrum in (4) to the spectrum in Fig. 8. The least squares estimates of the free parameters of the model are the rms height of the topography, $(\overline{h^2})^{1/2} = 155$ m; the characteristic wavenumber $\kappa_0 = 1.2 \times 10^{-4}$ m^{-1}; and the high-wavenumber slope $\mu = 3.5$. The model spectrum seems to capture well the drop in the topographic spectrum at small wavenumbers and provides the required extrapolation to small scales.

3. Energy radiation theory

A geostrophic eddy flowing over small-scale finite-amplitude topography can radiate internal gravity waves. Residual mean theory (Andrews and McIntyre 1976) shows that the upward-radiating internal waves feedback on the geostrophic flow through the divergence of the Eliassen–Palm (E–P) flux. The vertical component

TABLE 1. Ship surveys.

	Institution	Survey year	Ship name	Bathymetry instrumentation	Resolution (m)
1	LDEO	1965	*Eltanin*	12-kHz PDR widebeam	300–850
2	LDEO	1969	*Hudson*		370
3	SIO	1984	*T. Washington*	Seabeam vertical beam	350–450
4	LDEO	1966	*Eltanin*	12-kHz PDR widebeam	1200–1800
5	SIO	1998	*Nathaniel B. Palmer*	Seabeam 2112	300–500
6	LDEO	1960	*Vema*	12-kHz PDR widebeam	600–1200
7	LDEO	1964	*Eltanin*	12-kHz PDR widebeam	200–1500
8	LDEO	1965	*Eltanin*	12-kHz PDR widebeam	200–3000

LDEO = Lamont-Doherty Earth Observatory; SIO = Scripps Institution of Oceanography.

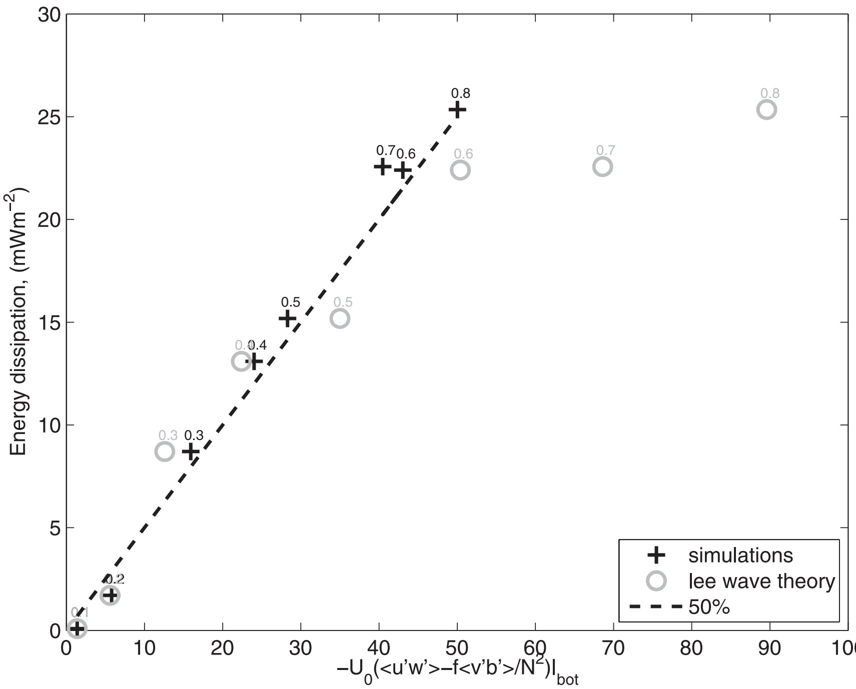

FIG. 9. The work extracted by waves from the mean flow, $-U_0(\overline{w'u'} - f\overline{v'b'}/N^2)|_{\text{bot}}$, vs the vertical integral of energy dissipation, $E = \int \varepsilon\, dz = \int \nu|\nabla \mathbf{u}|^2\, dz$, for a suite of numerical simulations with different nonlinear parameters ϵ (indicated next to each cross–circle). Crosses indicate results when both quantities are estimated from numerical simulations and circles show results when the work extracted by waves is estimate from linear lee wave theory. The dashed line has a slope of ½, suggesting that 50% of the energy extracted by the waves is locally dissipated. Estimates based on linear lee wave theory diverge from the dashed line for $\epsilon > 0.7$ due to energy radiation saturation. Linear lee wave theory overestimates the energy radiation for $\epsilon > 0.7$.

of the E–P flux for internal gravity waves is $F_z = \overline{w'u'} - f\overline{v'b'}/N^2$.

Nikurashin and Ferrari (2010) found that the E–P flux divergence associated with the internal waves drives strong inertial oscillations (IOs) confined to a few hundred meters from the ocean bottom. The IOs provide a background shear that promotes wave breaking so that a large fraction of the internal wave pseudomomentum (Bühler 2009) is deposited where the E–P flux diminishes within a few hundred meters of the bottom topography—for the parameter space considered in this paper, the pseudomomentum is well approximated by the traditional momentum. The deposition of internal wave pseudomomentum results in a dissipation ε of about 50% of the wave energy radiated from the bottom topography (i.e., $E = \int \varepsilon\, dz \approx -1/2U_0(\overline{w'u'} - f\overline{v'b'}/N^2)|_{z=0}$), as shown in Fig. 9. This empirical relationship is the cornerstone for the estimates of wave energy dissipation presented in this paper.

Nikurashin and Ferrari (2010) show that linear lee wave theory provides a good estimate of the E–P flux; the presence of IOs in the bottom flow modifies radiation by less than 15%. Linear lee wave theory can then be used to relate the E–P flux to the wave energy flux:

$$\overline{p'w'} = -U_0(\overline{w'u'} - f\overline{v'b'}/N^2). \tag{5}$$

This relationship is very useful, because the wave energy flux is a quantity more directly accessible from observations, but the E–P flux is more fundamental from a dynamical point of view. Andrews and McIntyre (1976) show that the divergence of the E–P flux, and not the divergence of the momentum flux, represents the full force exerted on the mean flow by the waves as they break and dissipate. Neglecting a small correction due to IOs, the wave radiation reduces to the classical lee wave problem discussed by Bell (1975a,b). However, IO shear is crucial to our assumption that 50% of the radiated energy is locally dissipated. In the linear lee wave problem, no wave breaking occurs and $E = 0$.

a. *Lee wave radiation*

Internal lee waves are generated in a stratified fluid when a steady geostrophic flow runs over uneven bottom topography. Bell (1975a,b) shows that the energy radiated in steady lee waves is given by

$$E = \frac{\rho_0}{4\pi^2}\int_{-\infty}^{+\infty}\int_{-\infty}^{+\infty}\frac{(\mathbf{U}_0\cdot\mathbf{k})}{|\mathbf{k}|}P(\mathbf{k})\sqrt{(\mathbf{U}_0\cdot\mathbf{k})^2 - f^2}\sqrt{N^2 - (\mathbf{U}_0\cdot\mathbf{k})^2}\,d\mathbf{k}, \tag{6}$$

where $P(\mathbf{k})$ is the 2D topography spectrum, $\mathbf{k} = (k, l)$ is the wavenumber vector, $\mathbf{U}_0$ is the bottom velocity vector, N the bottom stratification, f the Coriolis frequency, and ρ_0 a reference density. This result applies for wavenumbers in the radiation range, as given in (1), and at a small topographic steepness parameter:

$$\epsilon_0 = \frac{Nh}{|\mathbf{U}_0|}, \tag{7}$$

where h is a characteristic topographic height. The definitions of h found in the literature are quite arbitrary for topography with hills on many scales, and we return to this point below. Nikurashin and Ferrari (2010) showed that, for monochromatic topography where h is the amplitude of the sinusoidal bump, the linear theory prediction remains accurate until $\epsilon_c = 0.7$. For $\epsilon_0 > \epsilon_c$, the energy conversion saturates; that is, it ceases to increase as a function of ε_0, due to topographic blocking effects.

Expression (6) predicts that energy radiation at each wavenumber depends on the topographic elevation at that scale and the relative orientation of the velocity and wavenumber vectors. Without loss of generality, we rotate the reference frame to have the velocity vector $\mathbf{U}_0$ along the k axis. Then, $\mathbf{U}_0 \cdot \mathbf{k} = |\mathbf{U}_0||k|$, and the expression (6) reduces to

$$E = \frac{\rho_0|\mathbf{U}_0|}{2\pi}\int_{|f|/|\mathbf{U}_0|}^{N/|\mathbf{U}_0|} dk\sqrt{|\mathbf{U}_0|^2k^2 - f^2}\sqrt{N^2 - |\mathbf{U}_0|^2k^2}\,\frac{1}{2\pi}\int_{-\infty}^{+\infty}\frac{|k|}{|\mathbf{k}|}P(\mathbf{k})\,dl, \tag{8}$$

where $\mathbf{k} = (k, l)$ is now the wavenumber in the reference frame along and across the mean flow. The outer integral on the right-hand side depends only on the wavenumber k in the direction of the mean flow vector and includes contributions from wavenumbers in the radiative range. The inner integral, on the other hand, does not depend on the properties of the mean flow. It depends only on the properties of the topography spectrum and can be integrated over all wavenumbers in the direction across the mean flow velocity vector. It is convenient to define the effective one-dimensional topography spectrum in wavenumber k as

$$P_{\text{eff}}(k) = \frac{1}{2\pi}\int_{-\infty}^{+\infty}\frac{|k|}{|\mathbf{k}|}P(\mathbf{k})\,dl. \tag{9}$$

Then wave radiation from two-dimensional topography reduces to an equivalent one-dimensional wave radiation problem in the direction along the mean flow with the topography spectrum given by $P_{\text{eff}}(k)$. The energy conversion can now be rewritten in the following form as an integral in the wavenumber k:

$$E = \frac{\rho_0|\mathbf{U}_0|^3}{\pi}\int_{|f|/|\mathbf{U}_0|}^{N/|\mathbf{U}_0|} kP_{\text{eff}}(k)m(k)\left(1 - \frac{f^2}{|\mathbf{U}_0|^2k^2}\right)dk, \tag{10}$$

where $m(k)$ is the internal wave vertical wavenumber defined as

$$m(k) = k\sqrt{\frac{N^2 - |\mathbf{U}_0|^2k^2}{|\mathbf{U}_0|^2k^2 - f^2}}. \tag{11}$$

Equation (10), together with the effective topography spectrum defined in (9), constitute the building blocks for our estimates of wave radiation from data.

b. *Simplified theory*

The expression for the energy conversion in (10) is quite opaque. Making a few additional assumptions about the shape of the topography spectrum, and the ratio of frequencies f and N, the expression can be substantially simplified. As we show below, the additional assumptions are well satisfied in the regions considered in this study.

First, let us assume that the model spectrum in (3) is isotropic (i.e., $k_0 = l_0 = \kappa_0$) and that internal waves radiate from topography scales such that $|\mathbf{k}|^2 \gg \kappa_0^2$. Then, P_{eff} in (9) becomes

$$P_{\text{eff}}(k) = P_0k^{-(\mu-1)}, \tag{12}$$

where

$$P_0 = \overline{h^2}\kappa_0^{\mu-2}(\mu - 2)B\left(\frac{1}{2}, \frac{\mu}{2}\right), \tag{13}$$

and $B(1/2, \mu/2)$ is the beta function.

This approximation captures both the magnitude and slope of the spectrum at the high wavenumbers that dominate wave radiation. Plugging the effective topography spectrum (12) into the energy conversion expression (10), we get

$$E = \frac{1}{\pi}\rho_0 P_0 N|\mathbf{U}_0|^2 \frac{|\mathbf{U}_0|^{(\mu-3)}}{N^{(\mu-3)}} \int_{|f|/N}^{1} t^{2-\mu}(1-t^2)^{1/2}\left(1-\frac{f^2}{N^2}t^{-2}\right)^{1/2} dt, \tag{14}$$

where t is the new variable of integration given by

$$t = \frac{|\mathbf{U}_0|}{N}k. \tag{15}$$

Expanding the two square roots in their Taylor series, the integral on the right-hand side can be evaluated analytically for arbitrary μ (see the appendix for details). Setting $\mu = 3.5$, the value that characterizes the topography in the two regions considered in this paper, and assuming that $|f|/N \ll 1$, we get a simplified expression for the energy conversion at the ocean bottom:

$$E \approx \frac{1}{\pi}\rho_0 P_0 N|\mathbf{U}_0|^2 \frac{|\mathbf{U}_0|^{1/2}}{|f|^{1/2}}\left[\frac{9}{5} - \frac{7}{3}\sqrt{\frac{|f|}{N}} + O\left(\frac{f^2}{N^2}\right)\right]. \tag{16}$$

Expression (16) can be compared with the equivalent expression for radiation by a monochromatic topography: $E = 1/2\rho_0 h^2 kNU^2$. If we define the mean product of the height squared and the wavenumber $\overline{h^2k}|_{\mathrm{LW}}$ characteristic of the lee wave wavenumber range as

$$\begin{aligned}\overline{h^2k}|_{\mathrm{LW}} &= \frac{1}{\pi}\int_{|f|/|\mathbf{U}_0|}^{N/|\mathbf{U}_0|} kP_{\mathrm{eff}}(k)\,dk \\ &= \frac{2P_0}{\pi}\frac{|\mathbf{U}_0|^{1/2}}{|f|^{1/2}}\left(1-\sqrt{\frac{|f|}{N}}\right),\end{aligned} \tag{17}$$

then expression (16) takes the form

$$E = \frac{1}{2}\rho_0 \overline{h^2k}|_{\mathrm{LW}} N|\mathbf{U}_0|^2 \frac{\left[\frac{9}{5}-\frac{7}{3}\sqrt{\frac{|f|}{N}}+O\left(\frac{f^2}{N^2}\right)\right]}{\left(1-\sqrt{\frac{|f|}{N}}\right)}. \tag{18}$$

To leading order, the energy radiation by multichromatic topography can be understood as radiation from a monochromatic bump with topographic characteristics given by $\overline{h^2k}|_{\mathrm{LW}}$. However, as per (17), $\overline{h^2k}|_{\mathrm{LW}}$ depends on $|\mathbf{U}_0|^{1/2}$ instead of being constant. The implication is that the energy radiation is proportional to $|\mathbf{U}_0|^{5/2}$ for multichromatic topography, but it is proportional to $|\mathbf{U}_0|^2$ for monochromatic topography. The different dependence in the multichromatic case is determined by the slope of the topographic spectrum, which determines the wavenumber range associated with lee wave radiation.

4. Estimates of energy radiation

The wave radiation expressions in (10) and (16) are now used to estimate the generation of internal gravity waves for the velocity and stratification data discussed above. Energy radiation is estimated for each station along the sections. It is assumed that the topography characteristics in the radiative range are uniform along each section for the two regions considered.

a. Steepness parameter estimate

Idealized numerical simulations with monochromatic topography (Nikurashin and Ferrari 2010) show that the characteristics and magnitude of the radiated waves are controlled by the steepness parameter, ϵ_0, defined in (7). The bottom energy radiation increases quadratically with ϵ_0, consistent with linear theory, for $\epsilon_0 \leq \epsilon_c$, where $\epsilon_c = 0.7$ is the critical steepness parameter. When ϵ_0 exceeds the critical value ϵ_c, some fraction of the flow becomes blocked by topography and energy radiation ceases to increase with ϵ_0. The interpretation is that the stagnant fluid in the troughs acts to reduce the effective topography seen by the flow.

An extension of the definition of the steepness parameter for waves of wavenumber $\mathbf{k}$ impinging on multichromatic topography is given by the ratio of the topographic slope in the direction of the wave to the slope of the wave:

$$\hat{\epsilon}(\mathbf{k}) = \frac{m(\mathbf{k})}{|\mathbf{k}|^2}[kS_x(\mathbf{k}) + lS_y(\mathbf{k})], \tag{19}$$

where $S_x(\mathbf{k})$ and $S_y(\mathbf{k})$ are the topographic slopes along and across the mean flow directions. The topographic slope at wavenumber $\mathbf{k}$ is given by the integral of the slope spectrum over all wavenumbers $\mathbf{k}'$ such that $|\mathbf{k}'| \leq |\mathbf{k}|$, that is, over the area of a circle of radius $|\mathbf{k}|$:

$$S_x(\mathbf{k}) = \left[\frac{2}{\pi^2}\int\int_{|\mathbf{k}'|\le|\mathbf{k}|} k'^2 P(k', l')\, dk'\, dl'\right]^{1/2},$$

$$S_y(\mathbf{k}) = \left[\frac{2}{\pi^2}\int\int_{|\mathbf{k}'|\le|\mathbf{k}|} l'^2 P(k', l')\, dk'\, dl'\right]^{1/2}.$$

The slopes have been normalized such that, in the limit of the monochromatic topography, $\epsilon = mh$, where h is the height of the sinusoidal hill. For monochromatic hills such that $|f| \ll |\mathbf{U}_0|k \ll N$, $m \simeq N/|\mathbf{U}_0|$, and this definition reduces to $\epsilon_0 = Nh/|\mathbf{U}_0|$, which is used, for example, to describe 2D idealized simulations in Nikurashin and Ferrari (2010).

To characterize the degree of nonlinearity of the whole spectrum of waves radiated from the multichromatic topography, a bulk ϵ is defined as the average of $\hat{\epsilon}(\mathbf{k})$ weighted by the corresponding energy radiation:

$$\epsilon = \frac{\int\int \hat{\epsilon}(\mathbf{k})E(\mathbf{k})\, dk\, dl}{\int\int E(\mathbf{k})\, dk\, dl}, \tag{20}$$

where $E(\mathbf{k})$ is the spectrum of energy radiation, that is, the integrand in Eq. (8). The weighting by the energy radiation is included to focus the definition of ϵ on the waves that most matter for radiation. The definition is somewhat arbitrary, but it captures the transition from linear to nonlinear behavior, as we show with numerical simulations in section 5.

Figure 10 shows ϵ estimated from (20) for the sections across Drake Passage and in the southeast Pacific. The southeast Pacific section is characterized by smaller values of ϵ of about 0.2–0.3. In Nikurashin and Ferrari (2010) and in section 5 it is shown that for this ϵ range the radiation is mostly in the form of quasi-stationary lee waves. In Drake Passage, however, ϵ spans the range 0.3–0.5 south of 60.5°S and 0.5–1.1 north of it. These steepness parameter values correspond to a time-dependent wave radiation regime associated with vigorous IOs and wave breaking in the bottom 1 km. We note that ϵ is lower in the South ACC Front than in the Polar Front mostly because of the lower values of N in the southern Drake Passage. In the Polar Front, at 59°S, which accounts for the bulk of radiation, ϵ is roughly 0.6–0.8.

To summarize, ϵ in the two regions of the Southern Ocean considered in this study varies from $\simeq$0.2 to 1.0, spanning subcritical and critical topography. Numerical simulations with monochromatic topography (Nikurashin and Ferrari 2010) and multichromatic topography (section 5) show that this range of ϵ spans the transition from the radiation of stationary lee waves ($\epsilon \ll 1$) to the radiation of time-dependent waves ($\epsilon \le \epsilon_c$). Numerical experiments show that the bottom value of the energy flux is well predicted by linear theory for both wave radiation regimes: $\epsilon \le \epsilon_c$. Radiation levels do not further increase for $\epsilon \ge \epsilon_c$. It appears that ϵ_c is close to 0.7 for the multichromatic topography characteristics of the region considered in this study (section 5). The value of ϵ estimated from observations exceeds this critical value in the Drake Passage for the stations between the fronts of the ACC where bottom velocity is small. Thus, energy radiation computed for the Drake Passage region using linear theory (Bell 1975a,b; Nycander 2005) might be somewhat overestimated. We return to this issue in section 6 where we present numerical simulations for multichromatic topography.

b. *Effective topography spectrum*

We estimate the effective spectrum P_{eff} defined in (9) by using the 2D model spectrum in (3) and integrating it over all wavenumbers across the direction of the flow. In the Drake Passage region, the parameters of the 2D model spectrum are estimated by a least squares fit to the 2D topography data. In the southeast Pacific, only 1D topographic sections are available, and the 2D spectral representation (i.e., the degree of anisotropy) cannot be uniquely determined; we will resort to estimating the uncertainty associated with plausible ranges of anisotropy.

To estimate P_{eff}, we proceed as follows. First, we assume that the geostrophic flow can come at any angle with respect to the topography. The kinetic energy in the geostrophic velocity field is dominated by transient eddies, whose velocity direction is very variable and can span the whole 360° over a few eddy turnover times. Rather than estimating energy radiation for a particular velocity realization, we estimate radiation for two limiting cases, that is, for flows going across and along the major axis of the topographic spectrum. The two estimates provide the lower and the upper limits of wave energy radiation and, thus, define the uncertainty due to the variable orientation between the flow and topography.

Drake Passage estimates of the effective spectrum are shown in Fig. 11. The spectrum has a roll off with $\mu = 3.5$ in the lee wave radiation wavenumber range. The weak anisotropy in topography (ratio of major to minor axis of 1.8) results in about a factor of 3 difference between the lower and the upper limits of the effective spectrum.

In the southeast Pacific, we must additionally estimate how sensitive P_{eff} is to the undetermined degree of anisotropy in the topography. As a starting point, we assume that the topography aspect ratio, a, is similar to that in the Drake Passage region ($a \simeq 1.8$). In both the southeast Pacific and Drake Passage regions, the topography at scales larger than 50–100 km is dominated by ridges

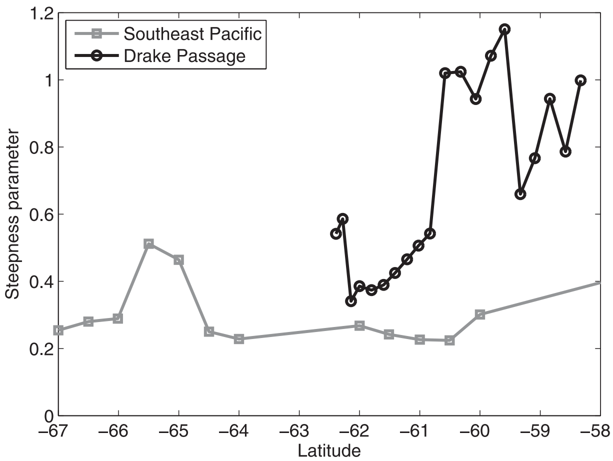

FIG. 10. Steepness parameter estimates for the Drake Passage (black) and the southeast Pacific (gray) regions. The steepness parameter ϵ from multichromatic topography is defined in (20).

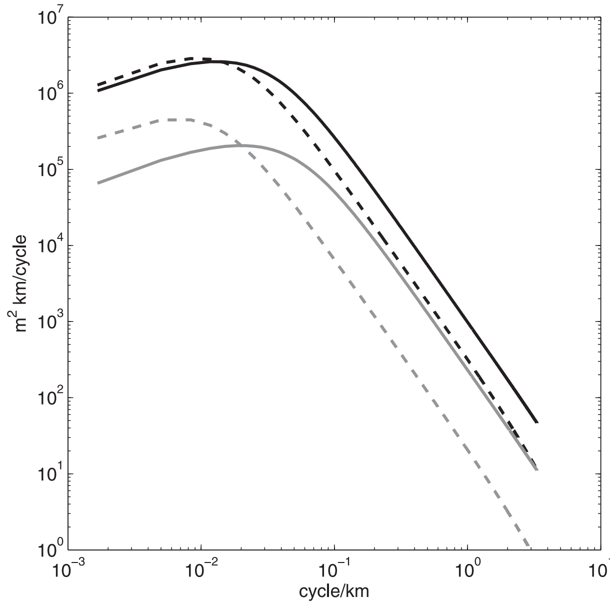

FIG. 11. Effective topographic spectra for the Drake Passage region (black) and the southeast Pacific region (gray). The solid and dashed curves represent the lower and upper bounds due to the unknown topographic anisotropy and uncertainties in the relative orientation between the topography and the mean flow.

with similar characteristics. Since topographic features formed at ridged crests tend to elongate perpendicular to the direction of spreading in a self-similar fashion (Goff and Jordan 1988), it seems reasonable to assume that the spectral roll offs are similar in the two regions. As a second case, we estimate the radiation for an isotropic topography with $a = 1$ to quantify the effects of the uncertainties in the topographic anisotropy.

There is, in general, an infinite number of ellipses characterized by the same ratio of major to minor axes of anisotropy a and the same characteristic wavenumber in a certain direction κ_0. However, the minor and the major axes of these ellipses are bounded: the minor axis of an ellipse cannot be smaller than κ_0/a and the major axis cannot be greater than $a\kappa_0$, if the ellipse is to have κ_0 as a characteristic wavenumber in a certain direction. Hence, the lower and upper radiation limits correspond, respectively, to the flow along the minor axis of the ellipse $(\kappa_0, a^{-1}\kappa_0)$, that is, along κ_0/a, and along the major axis of the ellipse $(a\kappa_0, \kappa_0)$, that is, along $a\kappa_0$. Estimates of P_{eff} for the southeast Pacific are shown in Fig. 10. The lower and the upper limits differ by a factor of about 10–12 in the lee wave radiation range. The greater degree of uncertainty in the southeast Pacific region arises from uncertainties in both the flow orientation and the degree of topographic anisotropy. For all flow orientations and the degree of topographic anisotropy P_{eff} is greater in Drake Passage than in the southeast Pacific region.

c. *Energy radiation estimate*

We estimate energy radiation in both regions using the best-fit effective topography spectrum together with measurements of bottom velocity and stratification. We report results from three different calculations: (i) E_{full} computed from the full expression for energy radiation in (10) and the anisotropic spectrum in (3), where the upper and lower limits correspond to flows along the major and minor axes of the topographic spectrum, respectively; (ii) E_{iso} estimated assuming that the spectra are isotropic; and (iii) E_{sim} estimated with the simplified expression in (16).

Energy radiation estimates for the section in Drake Passage, uncorrected for finite steepness parameters, are shown in Fig. 12. The radiation varies strongly along the section. This spatial variability is determined by the bottom velocity and stratification distribution and has a maximum corresponding to the Polar Front of the ACC. In the South ACC Front, where the density stratification is half that in the Polar Front, the energy radiation is weaker. Weaker stratification results not only in smaller wave amplitudes but also in a narrower radiation wavenumber range as implied by (1). Values of energy radiation averaged along the section are in the range 14–42 mW m^{-2} where the lower and the upper limits correspond, respectively, to flows along and across elongated topographic hills.

Variations in the energy radiation estimate for an anisotropic spectrum are due to variations in the direction of the flow. We expect the eddy velocity to span all directions over time. Therefore, the best estimate of the time-average radiation is the mean between the

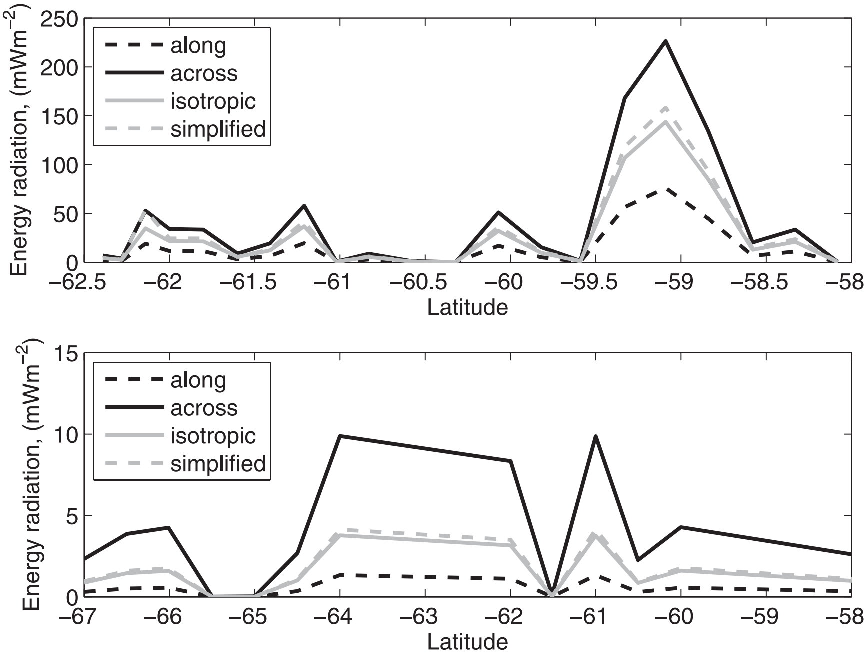

FIG. 12. Energy radiation estimates (mW m^{-2}) (top) along the ALBATROSS section in the Drake Passage and (bottom) along the P18 section in the southeast Pacific regions. The black curves (solid and dashed) bracket the range of uncertainty in the estimates, while the gray curves are a good approximation of the most likely values as described in section 4.

values computed for all possible flow directions (i.e., 28 mW m^{-2}).

Energy radiation computed using an isotropic spectrum falls between the lower and the upper limits for anisotropic topography. The isotropic spectrum estimate is $\simeq$27 mW m^{-2}; that is, it matches the anisotropic spectra estimate averaged over all possible flow directions. It appears that anisotropies in topography affect the instantaneous radiation, but over a few eddy turnover times the effect is smeared out by variations in the orientation of the geostrophic flow. The isotropic spectrum calculation and the simplified theory result also agree remarkably well in both regions (Fig. 12) supporting the assumptions made to simplify and evaluate the integral expression. The section-averaged energy radiation estimated using the isotropic spectrum is 27 mW m^{-2}. The simplified expression in (16) gives 30 mW m^{-2}.

We make the same three estimates along the section in the southeast Pacific region (Fig. 12). Energy radiation estimates are more than an order of magnitude smaller, mostly due to lower levels in the topography spectrum and, partly, because of somewhat lower values of bottom stratification and velocity. The energy radiation estimated using an anisotropic spectrum and averaged along the section is in the range 0.5–3.9 mW m^{-2}. The wide range in this estimate reflects the uncertainty in anisotropy, which adds to the uncertainty in flow orientation. The values averaged over all possible flow directions are 1 and 2.6 mW m^{-2} for the two realizations of anisotropic topography in (3) described, respectively, by two sets of characteristic wavenumbers: (κ_0, $a^{-1}\kappa_0$) and ($a\kappa_0$, κ_0). Estimates based on an isotropic spectrum and the simplified theory (16) produce 1.6 and 1.5 mW m^{-2}, respectively, for the section-averaged energy radiation. Radiation increases in the core of the ACC and drops to zero on its flanks.

5. Multichromatic topography simulations

The amount of observed energy dissipation and its spatial variation between the two regions seems to be well captured by the linear energy radiation estimate. However, the energy radiated by internal waves might not be all dissipated locally. Some fraction of that energy can radiate away in low modes and dissipate in remote regions. Idealized numerical simulations with monochromatic bottom topography (Nikurashin and Ferrari 2010) show that 50% of the radiated energy is locally dissipated in the bottom kilometer. In this section, we show that the result carries over to multichromatic topography.

a. Experiment setup

We use the nonhydrostatic configuration of the Massachusetts Institute of Technology general circulation model (MITgcm; Marshall et al. 1997). The numerical setup is similar to that used in the idealized simulations described in Nikurashin and Ferrari (2010). The domain is 2D and horizontally periodic with $L_x \times H_z = 10$ km $\times$ 7 km, somewhat larger than in our previous study to allow for different topographic wavenumbers. We use a resolution of $\Delta x = 16.6$ m in the horizontal and $\Delta z = 10$ m in the vertical, which gradually stretches to $\Delta z = 300$ m in the region from 2 to 7 km above the bottom. Boundary conditions are a sponge layer between 2 and 7 km above the bottom to absorb waves that do not break in the bottom 2 km, with a free-slip condition at the bottom. A depth-independent mean flow $U_G = 0.1$ m s^{-1} is forced by adding a body force fU_G to the meridional momentum equation representing a barotropic pressure gradient, which balances a mean flow geostrophically at all depths. A uniform stratification of $N = 10^{-3}$ s^{-1} and a Coriolis frequency of $f = 10^{-4}$ s^{-1} are used.

The bottom topography used in the simulations is randomly generated to have the same spectrum as in the observations, that is, the 1D model spectrum in (12). The random spectrum is computed as a sum of Fourier modes where amplitudes are given by the 1D model spectrum and the phases are random. Topography includes horizontal scales in the characteristic lee wave radiation range, which spans scales roughly from 600 m to 6 km, that is, only wavenumbers larger than the wavenumber $\kappa_0 = 1.2 \times 10^{-4}$ m^{-1}, below which the model spectrum (12) becomes flat. In the simulation of the southeast Pacific region, the topography amplitude is $\sqrt{10}$ smaller compared to the Drake Passage simulation, as estimated from topographic data. Corresponding nonlinear parameters ϵ as defined in (20) are 0.2 and 0.5 for the southeast Pacific and the Drake Passage simulations, respectively. In addition, we ran an extra simulation with $\epsilon = 0.75$ to demonstrate the suppression of energy radiation at higher ϵ.

b. Results

Snapshots of the wave zonal velocity component for the Drake Passage and the southeast Pacific regions after 5 days of simulations are shown in Fig. 13. The Drake Passage simulation is characterized by radiation of waves with 0.1 m s^{-1} amplitude, comparable in magnitude to the mean flow. As waves radiate away from the topography, they break and their amplitude drops by an order of magnitude within the bottom 1 km. The wave fields both close to the topography and in the far field are highly multichromatic and time dependent.

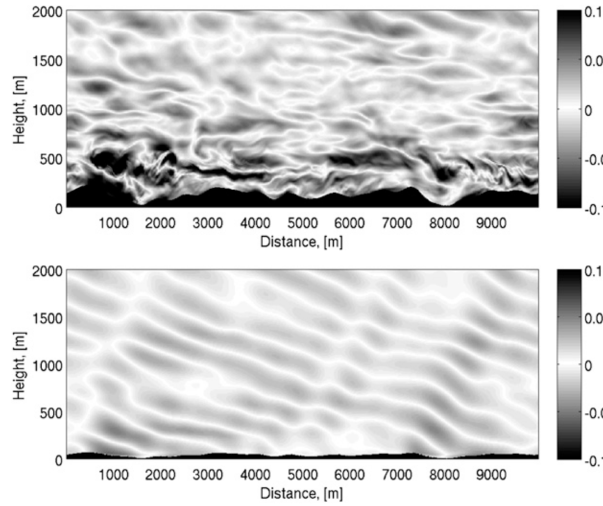

FIG. 13. Snapshot of the wave zonal velocity (m s^{-1}) from (top) the Drake Passage and (bottom) the southeast Pacific simulations.

In the southeast Pacific simulation, where the topography spectrum is an order of magnitude smaller, waves have a lower amplitude and do not decay significantly with height, radiating freely upward until they are absorbed in the sponge layer at the upper boundary. The velocity field is dominated by waves with horizontal scales of roughly 3 km with a weaker multichromatic background field due to different topographic scales. Waves are stationary and have scales that are consistent with linear steady lee wave theory.

The time evolution of the zonally averaged velocity is shown in Fig. 14 for the Drake Passage and the southeast Pacific regions. The Drake Passage simulation is characterized by vigorous IOs, which develop spontaneously and reach a magnitude comparable to the mean flow within the first 3–5 days. In the southeast Pacific simulation, instead, there are no IOs for the whole period of simulation. This result is consistent with the resonant feedback mechanism described in Nikurashin and Ferrari (2010) for $0.3 \le \epsilon \le 0.7$. Large-amplitude internal waves in the Drake Passage simulation drive a large momentum flux divergence and trigger IOs at the bottom. IOs in turn modify the wave generation process and produce time-dependent internal waves that can effectively reinforce IOs. The combination of large-amplitude waves and IOs leads to a new statistically steady state characterized by time-dependent waves and bottom-intensified IOs. In the southeast Pacific the feedback mechanism is weak (ϵ is small) and wave radiation is well described by linear lee wave theory.

Vertical profiles of the energy dissipation rate diagnosed from the simulations are shown in Fig. 15. The energy dissipation is an order of magnitude larger in

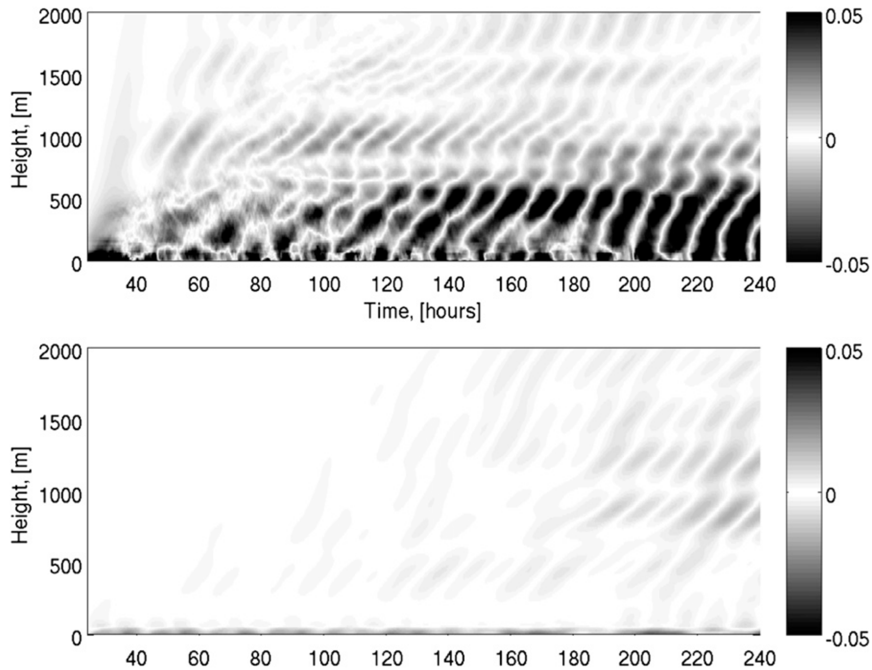

FIG. 14. Time evolution of the zonally averaged meridional velocity component (m s^{-1}) from (top) the Drake Passage and (bottom) the southeast Pacific simulations.

Drake Passage than in the southeast Pacific. Dissipation is significantly enhanced in the bottom several hundred meters in the Drake Passage simulation while it is nearly uniform in the southeast Pacific one. The total energy dissipation rates integrated into the bottom kilometer are 21 and 0.7 mW m^{-2}, respectively, in the two regions. Corresponding values of the pressure work, $-U_0(\overline{w'u'} - f\overline{v'b'}/N^2)$, due to the E–P stress at the bottom are 44 and 6.5 mW m^{-2}. These values are well predicted by the linear lee wave theory described above, which gives 45 and 6.3 mW m^{-2}, respectively. The energy dissipation diagnosed from the simulations is consistent with our theoretical estimates (section 4c) and with in situ observations (Naveira Garabato et al. 2004). The energy radiation in the southeast Pacific simulation is a factor of 2–3 higher than the corresponding estimates in section 4c, because stratification and velocity values, fixed between the simulations, are representative of the Drake Passage region and are larger than those in the southeast Pacific.

An additional simulation with $\epsilon = 0.75$ is qualitatively similar to the Drake Passage simulation ($\epsilon = 0.5$): zonally averaged flow is time dependent and the energy dissipation rate is strongly enhanced at the bottom. Internal wave energy radiation of 62 mW m^{-2} is accompanied by 27 mW m^{-2} of energy dissipation in the bottom kilometer. Linear theory predicts a higher value of 84 mW m^{-2}, for the energy radiation in this simulation. The mismatch between the simulation and linear theory at high ϵ is due to the suppression of energy radiation caused by the topographic blocking of the mean flow. At $\epsilon > \epsilon_c$, flow from the deep valley cannot overcome the topographic bumps and becomes blocked by topography. As a result, the effective amplitude of the topography radiating waves is reduced. Two simulations at intermediate ϵ (not shown) indicate that $\epsilon_c = 0.6$–0.7 for multichromatic simulations, which is consistent with $\epsilon_c = 0.7$ for monochromatic simulations described in Nikurashin and Ferrari (2010).

The ratio of energy dissipation integrated over the bottom kilometer to the amount of work due to the E–P stress at the bottom is ≈50% for $\epsilon \geq 0.5$, the parameter range of Drake Passage. It is significantly smaller, close to 10%, for the smaller ϵ encountered in the southeast Pacific simulation. This is consistent with the results of the monochromatic simulations (Nikurashin and Ferrari 2010): strong vertical shear associated with IOs promotes enhanced wave breaking and dissipation at $\epsilon \geq 0.3$, while at $\epsilon < 0.3$ no inertial shear develops and the waves do not break.

6. Estimates of energy dissipation

The steepness parameters estimated from the observations are in the range 0.2–0.3 and 0.5–1.0 in the southeast Pacific and the Drake Passage regions, respectively. According to the multichromatic numerical simulations,

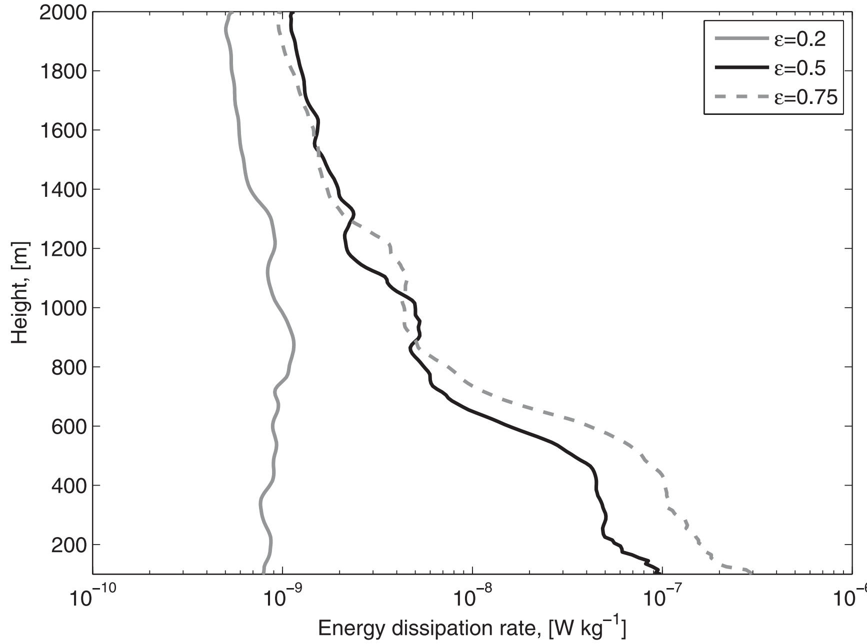

FIG. 15. Profiles of the energy dissipation rate (W kg^{-1}) diagnosed from the Drake Passage (solid black) and the southeast Pacific (solid gray) simulations, and a strongly nonlinear simulation (dashed gray). The nonlinear parameter that characterizes each simulation is given in the legend.

wave radiation is well described by the linear theory at $\epsilon < 0.7$ and saturates at higher values of ϵ. In the southeast Pacific, ϵ is below critical and the bottom energy radiation of 0.5–3.9 mW m^{-2} estimated from linear theory is accurate. However, in Drake Passage, ϵ exceeds the critical value ϵ_c in a few stations between fronts, where the bottom flow is weak. A correction to the estimate of 14–42 mW m^{-2} due to the suppression of energy radiation for $\epsilon > \epsilon_c$ is obtained by multiplying the energy radiation by $(\epsilon_c/\epsilon)^2$ for stations where $\epsilon > \epsilon_c$. This scaling accounts for the saturation of radiation at supercritical topography. It applies to monochromatic topography (Nikurashin and Ferrari 2010), but it appears to hold also for multichromatic topography. Applying this approach at every station along the section and averaging over all station, we estimate that saturation of energy radiation in those regions leads to a 15% reduction of the 14–42 mW m^{-2} estimate.

Numerical simulations with both monochromatic and multichromatic topography agree that 50% of the radiated energy is dissipated in the bottom kilometer for $\epsilon > 0.3$ and less than 10% at lower ϵ. Using energy radiation estimates from section 4c, we find that local energy dissipation is less than 2 mW m^{-2} in the southeast Pacific and 7–21 mW m^{-2} in the Drake Passage regions.

Our estimates of energy dissipation are on the same order as the 1 and 10 mW m^{-2} inferred from the observations by Naveira Garabato et al. (2004) and larger than those estimated by Kunze et al. (2006). The observations in Drake Passage are characterized by a higher strain–shear ratio than expected for the internal wave continuum. The same is true in our simulations as a result of IOs with strong shear but no strain. While Naveira Garabato et al. (2004) used the observed values of the strain–shear ratio to estimate the energy dissipation rate, Kunze et al. (2006) interpreted them as high levels of noise and low-pass filtered them. The agreement between our estimates and the ones by Naveira Garabato et al. (2004) suggests that the large strain–shear ratio could arise from the strong IOs above the bottom in regions with steep topography.

7. Conclusions

Recent estimates from LADCP observations show enhanced turbulent mixing in the Southern Ocean associated with internal wave breaking, which is typically concentrated in the bottom kilometer and has significant spatial variations. In this study we tested the hypothesis that this mixing can be sustained by internal waves generated by geostrophic eddies flowing over small-scale bottom topography. We applied linear wave radiation theory to the bottom topography, velocity, and stratification data from the southeast Pacific and the Drake

Passage regions characterized, respectively, by low and high rates of abyssal mixing. We showed that the estimated energy radiation and its spatial variations are consistent with the observations. Using numerical simulations with topographic characteristics representative of these two regions, we confirmed that ≈50% of the energy radiated by internal waves dissipates locally and sustains the energy dissipation observed in the bottom kilometer.

Section-averaged wave energy radiation is estimated to be 0.5–3.9 mW m^{-2} in the southeast Pacific region and 14–42 mW m^{-2} in the Drake Passage region. The lower and the upper limits of these two estimates are determined by the uncertainty in the flow orientation with respect to the anisotropy in the topography: flows across small-scale topographic features radiate more energy than flows along these features. Nikurashin and Ferrari (2010) and Fig. 9 show that only 50% of the energy radiation estimated from linear lee wave theory dissipates locally. Hence, our best estimate for local energy dissipation is less than 2 mW m^{-2} in the southeast Pacific and 7–21 mW m^{-2} in the Drake Passage region. These estimates are on the same order as the 1 mW m^{-2} and 10 mW m^{-2} of energy dissipation estimated from the observations in these two regions by Naveira Garabato et al. (2004) and somewhat larger than those estimated by Kunze et al. (2006).

Our work shows that energy radiation varies substantially across the ACC. In Drake Passage it is strongly dominated by the Polar Front of the ACC. The South ACC Front has lower energy radiation, mostly due to the lower values of stratification. In the southeast Pacific region stratification does not change significantly along the section and the energy radiation tracks variations in the bottom velocity field. It is largest in the core of the ACC and drops down essentially to zero on its flanks.

We find that the substantial difference in energy radiation between the two regions considered results primarily from differences in topographic roughness (a factor of 4) and secondarily from differences in velocity and stratification (a factor of 2.5).

Linear theory and numerical simulations show that the wave energy radiation is proportional to the bottom value of the kinetic energy (KE) in geostrophic motions. Ferrari and Wunsch (2008) show that 80%–90% of the KE of the ocean is in geostrophic eddies generated by instabilities of the mean currents. From the perspective of our work, this implies that wave radiation is largely maintained by geostrophic eddies rather than by mean flows. The results further show that wave radiation and subsequent breaking are very sensitive to the small-scale topographic roughness. Since the topographic roughness is spatially variable in the ocean and geostrophic velocities change on the eddy turnover time scale, wave radiation and dissipation at the ocean bottom are predicted to be both spatially and temporally variable.

Finally, our work suggests that, in regions where abyssal flows are dominated by geostrophic eddies, there is a direct correlation between small-scale dissipation rates and the magnitude of the geostrophic eddy velocity. Such a correlation could be investigated with mooring data. Another direction for future research, discussed to some extent in the literature (Buhler and McIntyre 2005; Dewar and Killworth 1995; Polzin 2008) is to study the degree to which wave radiation extracts energy from the geostrophic eddy field.

Acknowledgments. We thank Eric Kunze, Kurt Polzin, and two anonymous reviewers for their useful comments. We thank Dr. Nycander for providing his tidal energy flux data. This research was supported by the National Science Foundation under Award OCE-6919248.

APPENDIX

Analytical Evaluation of the Integral

The integral on the right-hand side of (14) written as

$$I(\delta) = \int_{\delta}^{1} t^{2-\nu}(1-t^2)^{1/2}(1-\delta^2 t^{-2})^{1/2}\,dt, \qquad \text{(A1)}$$

where $\delta = f/N$, can be evaluated analytically for an arbitrary ν if we expand the two square roots in their Taylor series:

$$(1-t^2)^{1/2} = \sum_{m=0}^{\infty} \alpha_m^{1/2}(-1)^m t^{2m},$$

$$(1-\delta^2 t^{-2})^{1/2} = \sum_{n=0}^{\infty} \alpha_n^{1/2}(-1)^n \delta^{2n} t^{-2n},$$

where $\alpha_m^{1/2}$ and $\alpha_n^{1/2}$ are the binomial coefficients. Using Taylor expansions, the integral (A1) can be rewritten as

$$I(\delta) = \sum_{m=0}^{\infty}\sum_{n=0}^{\infty} \alpha_m^{1/2}\alpha_n^{1/2}(-1)^{(m+n)}\delta^{2n}\int_{\delta}^{1} t^{2m-2n+2-\nu}\,dt.$$

This integral can now be easily evaluated:

$$I(\delta) = \sum_{m=0}^{\infty}\sum_{n=0}^{\infty} \alpha_m^{1/2}\alpha_n^{1/2}\frac{(-1)^{(m+n)}}{(2m-2n+3-\nu)}(\delta^{2n} - \delta^{2m+3-\nu}).$$

Assuming that $\delta \ll 1$ and $3 < \nu < 5$, the leading-order terms are

$$I(\delta) \approx A\delta^{(3-\nu)} + B + \cdots,$$

where

$$A = \sum_{n=0}^{\infty} \alpha_n^{1/2} \frac{(-1)^n}{(2n - 3 + \nu)}, \quad B = \sum_{m=0}^{\infty} \alpha_m^{1/2} \frac{(-1)^m}{(2m + 3 - \nu)}.$$

REFERENCES

Andrews, D., and M. McIntyre, 1976: Planetary waves in horizontal and vertical shear: The generalized Eliassen–Palm relation and the mean zonal acceleration. *J. Atmos. Sci.,* **33,** 2031–2048.

Bell, T., 1975a: Lee waves in stratified flows with simple harmonic time dependence. *J. Fluid Mech.,* **67,** 705–722.

——, 1975b: Topographically generated internal waves in the open ocean. *J. Geophys. Res.,* **80,** 320–327.

Bühler, O., 2009: *Waves and Mean Flows*. Cambridge University Press, 341 pp.

——, and M. McIntyre, 2005: Wave capture and wave–vortex duality. *J. Fluid Mech.,* **534,** 67–95.

Dewar, W., and P. Killworth, 1995: Do fast gravity waves interact with geostrophic motions? *Deep-Sea Res. I,* **42,** 1063–1081.

Egbert, G., and S. Erofeeva, 2002: Efficient inverse modeling of barotropic ocean tides. *J. Atmos. Oceanic Technol.,* **19,** 183–206.

Ferrari, R., and C. Wunsch, 2008: Ocean circulation kinetic energy—Reservoirs, sources and sinks. *Annu. Rev. Fluid Mech.,* **41,** 253–282.

Ganachaud, A., and C. Wunsch, 2000: Improved estimates of global ocean circulation, heat transport and mixing from hydrographic data. *Nature,* **408,** 453–456.

Garrett, C., and E. Kunze, 2007: Internal tide generation in the deep ocean. *Annu. Rev. Fluid Mech.,* **39,** 57–87.

Goff, J., and T. Jordan, 1988: Stochastic modeling of seafloor morphology: Inversion of sea beam data for second-order statistics. *J. Geophys. Res.,* **93,** 13 589–13 608.

Gregg, M., 1989: Scaling turbulent dissipation in the thermocline. *J. Geophys. Res.,* **94,** 9686–9698.

Heywood, K., and D. Stevens, 2000: Albatross cruise report. UEA Cruise Rep. Series 6, University of East Anglia, Norwich, United Kingdom, 61 pp.

Ito, T., and J. Marshall, 2008: Control of lower-limb circulation in the Southern Ocean by diapycnal mixing and mesoscale eddy transfer. *J. Phys. Oceanogr.,* **38,** 2832–2845.

Khatiwala, S., 2003: Generation of internal tides in an ocean of finite depth: Analytical and numerical calculations. *Deep-Sea Res. I,* **50,** 3–21.

Kunze, E., E. Firing, J. Hummon, T. Chereskin, and A. M. Thurnherr, 2006: Global abyssal mixing inferred from lowered ADCP shear and CTD strain profiles. *J. Phys. Oceanogr.,* **36,** 1553–1576.

Ledwell, J., E. Montgomery, K. Polzin, L. St. Laurent, R. Schmitt, and J. Toole, 2000: Evidence for enhanced mixing over rough topography. *Nature,* **403,** 179–182.

Llewellyn Smith, S., and W. Young, 2002: Conversion of the barotropic tide. *J. Phys. Oceanogr.,* **32,** 1554–1566.

Marshall, J., and T. Radko, 2003: Residual mean solutions for the Antarctic circumpolar current and its associated overturning circulation. *J. Phys. Oceanogr.,* **33,** 2341–2354.

——, A. Adcroft, C. Hill, L. Perelman, and C. Heisey, 1997: A finite-volume, incompressible Navier–Stokes model for studies of the ocean on parallel computers. *J. Geophys. Res.,* **102,** 5753–5766.

Naveira Garabato, A., K. Heywood, and D. Stevens, 2002: Modification and pathways of Southern Ocean deep waters in the Scotia Sea. *Deep-Sea Res.,* **49,** 681–705.

——, D. Stevens, and K. Heywood, 2003: Water mass conversion, fluxes, and mixing in the Scotia Sea diagnosed by an inverse model. *J. Phys. Oceanogr.,* **33,** 2565–2587.

——, K. Polzin, B. King, K. Heywood, and M. Visbeck, 2004: Widespread intense turbulent mixing in the Southern Ocean. *Science,* **303,** 210–213.

Nikurashin, M., and R. Ferrari, 2010: Radiation and dissipation of internal waves generated by geostrophic flows impinging on small-scale topography: Theory. *J. Phys. Oceanogr.,* **40,** 1055–1074.

Nowlin, W., J. Bottero, and R. Pillsbury, 1986: Observations of internal and near-inertial oscillations at Drake Passage. *J. Phys. Oceanogr.,* **16,** 87–108.

Nycander, J., 2005: Generation of internal waves in the deep ocean by tides. *J. Geophys. Res.,* **110,** C10028, doi:10.1029/2004JC002487.

Olbers, D., D. Borowski, C. Volker, and J. Wolff, 2004: The dynamical balance, transport and circulation of the Antarctic circumpolar current. *Antarct. Sci.,* **16,** 439–470.

Polzin, K. L., 2008: Mesoscale eddy–internal wave coupling. Part I: Symmetry, wave capture, and results from the Mid-Ocean Dynamics Experiment. *J. Phys. Oceanogr.,* **38,** 2556–2574.

——, and E. Firing, 1997: Estimates of diapycnal mixing using LADCP and CTD data from I8S. *WOCE International Newsletter,* No. 29, WOCE International Office, Southampton, United Kingdom, 29–42.

——, J. M. Toole, and R. W. Schmitt, 1995: Finescale parameterizations of turbulent dissipation. *J. Phys. Oceanogr.,* **25,** 306–328.

——, J. Toole, J. Ledwell, and R. Schmitt, 1997: Spatial variability of turbulent mixing in the abyssal ocean. *Science,* **276,** 93–96.

Rintoul, S., C. Hughes, and D. Olbers, 2001: The Antarctic circumpolar current system. *Ocean Circulation and Climate,* J. C. G. Siedler and J. Gould, Eds., Academic Press, 271–302.

Sloyan, B., and S. Rintoul, 2001: The Southern Ocean limb of the global deep overturning circulation. *J. Phys. Oceanogr.,* **31,** 143–173.

Smith, W., and D. Sandwell, 1997: Global seafloor topography from satellite altimetry and ship depth soundings. *Science,* **277,** 1957–1962.

Speer, K., S. Rintoul, and B. Sloyan, 2000: The diabatic Deacon cell. *J. Phys. Oceanogr.,* **30,** 3212–3222.

St. Laurent, L., and C. Garrett, 2002: The role of internal tides in mixing the deep ocean. *J. Phys. Oceanogr.,* **32,** 2882–2899.

Wunsch, C., 1997: The vertical partition of oceanic horizontal kinetic energy. *J. Phys. Oceanogr.,* **27,** 1770–1794.

——, and R. Ferrari, 2004: Vertical mixing, energy, and the general circulation of the ocean. *Agric. For. Meteor.,* **36,** 281–314.